Characterization of an Amorphous Iridium Water-Oxidation Catalyst Electrodeposited from Organometallic Precursors

James D. Blakemore,[†,⊥] Michael W. Mara,[‡,§] Maxwell N. Kushner-Lenhoff,[†] Nathan D. Schley,[†]
Steven J. Konezny,[†] Ivan Rivalta,[†,⊗] Christian F. A. Negre,[†] Robert C. Snoeberger,[†] Oleksandr Kokhan,[§]
Jier Huang,[§] Andrew Stickrath,[§] Lan Anh Tran,[∥] Maria L. Parr,[∥] Lin X. Chen,*[,‡,§] David M. Tiede,*[,§]
Victor S. Batista,*[,†] Robert H. Crabtree,*[,†] and Gary W. Brudvig*[,†]

[†]Department of Chemistry, Yale University, P.O. Box 208107, New Haven, Connecticut 06520-8107, United States
[‡]Department of Chemistry, Northwestern University, 2145 Sheridan Road, Evanston, Illinois 60208-3113, United States
[§]Chemical Sciences and Engineering Division, Argonne National Laboratory, Argonne, Illinois 60439, United States
[∥]Department of Chemistry, Trinity College, 300 Summit Street, Hartford, Connecticut 06106, United States

Ⓢ *Supporting Information*

ABSTRACT: Upon electrochemical oxidation of the precursor complexes [Cp*Ir(H$_2$O)$_3$]SO$_4$ (**1**) or [(Cp*Ir)$_2$(OH)$_3$]-OH (**2**) (Cp* = pentamethylcyclopentadienyl), a blue layer of amorphous iridium oxide containing a carbon admixture (**BL**) is deposited onto the anode. The solid-state, amorphous iridium oxide material that is formed from the molecular precursors is significantly more active for water-oxidation catalysis than crystalline IrO$_2$ and functions as a remarkably robust catalyst, capable of catalyzing water oxidation without deactivation or significant corrosion for at least 70 h. Elemental analysis reveals that **BL** contains carbon that is derived from the Cp* ligand (∼ 3% by mass after prolonged electrolysis). Because the electrodeposition of precursors **1** or **2** gives a highly active catalyst material, and electrochemical oxidation of other iridium complexes seems not to result in immediate conversion to iridium oxide materials, we investigate here the nature of the deposited material. The steps leading to the formation of **BL** and its structure have been investigated by a combination of spectroscopic and theoretical methods. IR spectroscopy shows that the carbon content of **BL**, while containing some C−H bonds intact at short times, is composed primarily of components with C=O fragments at longer times. X-ray absorption and X-ray absorption fine structure show that, on average, the six ligands to iridium in **BL** are likely oxygen atoms, consistent with formation of iridium oxide under the oxidizing conditions. High-energy X-ray scattering (HEXS) and pair distribution function (PDF) analysis (obtained ex situ on powder samples) show that **BL** is largely free of the molecular precursors and is composed of small, <7 Å, iridium oxide domains. Density functional theory (DFT) modeling of the X-ray data suggests a limited set of final components in **BL**; ketomalonate has been chosen as a model fragment because it gives a good fit to the HEXS-PDF data and is a potential decomposition product of Cp*.
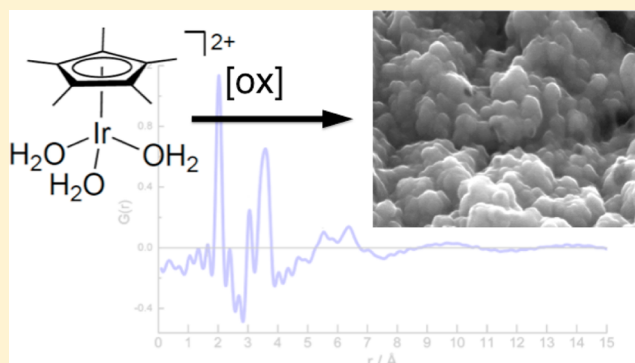
INTRODUCTION

The development of technologies for the production of chemical fuels with sunlight and inexpensive feedstocks relies on an abundant supply of protons and electrons to form the fuel.[1] Water is perhaps the best source of these protons and electrons, as water oxidation produces only oxygen gas as a byproduct:

$$2H_2O \rightarrow O_2 + 4H^+ + 4e^-$$
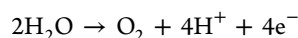
The water-oxidation reaction is both thermodynamically and kinetically demanding, having slow electrode kinetics even at high overpotentials without the use of a suitable catalyst. The sluggish kinetics are likely due to the many intermediates required to accomplish the complete 4H$^+$/4e$^-$ oxidation of water to dioxygen.

Among the catalysts known for water oxidation, iridium oxide-based materials offer both high activity and long-term stability.[2] Consequently, there has been great interest in understanding and improving preparations of iridium oxide. Dimensionally Stable Anodes, introduced more than half a century ago, proved the utility of iridium oxide materials in industrial settings.[3] Today, preparations of iridium oxide (with other noble and non-noble metals) perform water oxidation at high current densities in commercially available proton-exchange membrane (PEM) water electrolyzers.[4]

Traditional routes for the preparation of iridium oxide anodes can be grouped into three main categories. In the first, thermal decomposition of iridium chlorides on surfaces can give active oxide material.[5] In the second, iridium oxide nanoparticles can be synthesized in solution by hydrolysis of iridium precursors.[6] These nanoparticles can then be mechanically deposited onto electrodes, or electrodeposited. Murray's group[7] has used the latter method and obtained remarkably low overpotentials for water oxidation; the high activity of their assembled material likely relies on both the high intrinsic activity of iridium oxide and the high surface area of the small nanoparticles. Mallouk's group has also extensively investigated the formation and electrodeposition of iridium oxide nanoparticles,[8] and their use in more complex systems,[9] including one notably designed to achieve light-driven water oxidation.[10] In the third route to iridium oxide anodes, iridium metal can be oxidized to form amorphous iridium oxide,[11] which functions as a remarkably active catalyst for water oxidation.[12] A notable variant of this route is sputtering of iridium onto electrodes,[13] which gives remarkably active oxide material. These amorphous iridium oxides from the third route are often electrochromic,[14] a property afforded by an internal redox event of the stable oxide material.[15]

Recently, the use of iridium complexes as water-oxidation catalysts has attracted significant attention.[16] In our group, we have been exploring the chemistry of a number of half-sandwich iridium complexes for use as water-oxidation catalysts.[17] Depending on the ligands bound to iridium in addition to the pentamethylcyclopentadienyl (Cp*) ligand, we find that the complexes can either homogeneously oxidize water or the starting complex can form a heterogeneous material that also functions as a catalyst for the reaction. Specifically, we have found that electrochemical oxidation of $[Cp*Ir(H_2O)_3]SO_4$ (**1**) or $[(Cp*Ir)_2(OH)_3]OH$ (**2**) (Figure 1) yields a catalytically
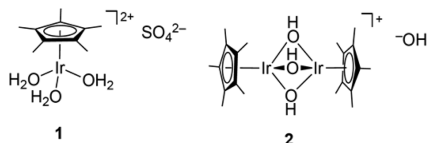
Figure 1. Structures of the iridium(III) complexes.

active heterogeneous material visible as a blue layer (**BL**) on the electrode.[18] In our preliminary work, we found that the catalyst clearly contained a carbon admixture which arises from the Cp* ligand in the starting complexes.

This interconversion between an organometallic (or, in analogous cases, inorganic) precursor and a heterogeneous oxide material that acts as the true catalyst is a unique test case where the ambiguity between homogeneous and heterogeneous water oxidation catalysis can be clarified. Because water oxidation is a thermodynamically and kinetically demanding reaction, the use of inorganic coordination complexes or organometallic complexes as molecular catalysts poses unique challenges; this is especially true in cases where the metals used in the "homogeneous" catalysts are highly active in their heterogeneous oxide forms. We have long been interested in this problem,[19] and have recently developed a new electrochemical method[20] based on a quartz crystal nanobalance (or microbalance) to distinguish between homogeneous and heterogeneous electrode-driven catalysis. In the case of complexes **1** and **2** discussed here, the organometallic

precursors are clearly converted to a secondary iridium oxide material, which functions as the true catalyst. Because this secondary material shows excellent activity for water oxidation, we have been interested in gaining more information about the structure of the catalyst. Moreover, we desired to clarify the role and ultimate fate of the carbon-containing Cp* ligand, because simple iridium salts and other iridium complexes we have tested do not electrodeposit like complexes **1** and **2**.[17,20,21]

Macchioni's group has investigated changes that may occur when Cp*Ir complexes bearing an additional bidentate chelate ligand are chemically oxidized.[22] Specifically, NMR data suggest that nucleophilic attack occurs on the Cp* ligand, resulting in substitution and further oxidation of the ligand. Treatment of the complexes with cerium(IV) ammonium nitrate[22a] (a strong one-electron oxidant) or hydrogen peroxide[22b] gives similar attack on the Cp* ring. Mayer's group[23] has also studied oxidation of the $[Cp*IrCl_2]_2$ dimer; in these experiments, treatment of the dimer with $PhI(OAc)_2$ results in oxidation of a Cp* methyl group to give the acetoxylated product. Under our electrochemical conditions, it is conceivable that similar routes to oxidized material may be operative because ligand oxidation processes likely occur via oxidized iridium intermediates.[17c] Finally, recent work from Lin's group[24] has examined the activity of Cp*Ir catalysts incorporated into metal−organic frameworks (MOFs) containing bidentate chelates and found that complete loss of Cp* can result from oxidation, but single-site catalysis can be retained with the modified ligand environment. Lin et al. do not detect CO_2 during the course of the reaction by headspace analysis, but can detect formation of acetate and formate in solution. In the case of **1** and **2**, oxidation of the complexes clearly results in formation of heterogeneous iridium oxide material (**BL**), which functions as the true catalyst for water oxidation.

Because **BL**, like other iridium materials, is highly active, and understanding the oxidative reactivity of these complexes is of current interest, we now report characterization of this electrodeposited material. DFT calculations (see the Supporting Information) of oxidation processess of the dimeric $[(Cp*Ir)_2(OH)_3]OH$ complex show that it can be oxidized to a manifold of higher oxidation states at potentials relevant to the chemistry we observe experimentally. This manifold of dimeric species is envisioned to aggregate or undergo further reactions; these oxidations and reactions may start the process of **BL** formation with the organometallic ligand set intact. Consistent with this hypothesis, IR spectroscopy of thin surface layers of **BL** suggests that some C−H bonds are intact *on the surface of the electrode* at short times. However, upon initiation of water electrolysis, (1) the C−H bonds are rapidly lost, (2) C=O fragments are formed, but (3) no deactivation of catalyst is observed. Thus, there must not be any direct Ir−C bonds at the active site of the catalyst once deposited on the surface.

Because the deposited material is completely amorphous and insoluble, we turned to in situ X-ray absorption spectroscopy (XAS) and ex suty high-energy X-ray scattering (HEXS) methods to gain more information about the structure and bonding in **BL**. XAS is an element-specific, short-range technique for determining the local structure around a specific atom with a resolution of 0.01−0.02 Å.[25] Furthermore, this technique can be applied to systems in various media, including films.[26] The X-ray absorption near-edge structure (XANES) region contains information on the local geometry and the oxidation state of the absorbing atom, while the extended X-ray absorption fine structure (XAFS) region contains information

on specific atom—atom distances. The oscillations in the absorption coefficient found in the XAFS region can be Fourier-transformed to obtain a pseudoradial distribution function, with Gaussian peaks representing the distances of the nearest scattering atoms from the absorbing atom.[27] XAFS can be particularly useful in studying bulk systems where the interesting dynamics occur around a unique atom, such as in transition metal complexes.[28]

X-ray scattering data complement these techniques by providing more information about the structure of **BL** beyond the first coordination shell. This is especially useful because **BL** is amorphous, and cannot be studied by more traditional X-ray diffraction methods. HEXS shows **BL** to consist of iridium oxide domains with maximum atomic pair correlations extending to 7 Å. DFT modeling of the XAFS and HEXS data confirms that the layer contains mostly oxo-bridged iridium species in the form of small domains of iridium oxide. Additionally, because the elemental analysis and spectroscopic data show the presence of carbon in the layer, ketomalonate (a potential decomposition product of Cp*) was modeled as a ligand to iridium for comparison with the experimental data. We find that this model organic fragment gives a good fit to the experimental spectroscopic data, but the actual identity of organic fragments in the layer remains unresolved.

■ RESULTS

Long Timecourse Activity and Elemental Analysis. As we have previously described,[18,20,29] electrochemical oxidation of **1** or **2** results in the formation of **BL** at the anode surface. This oxidation can be accomplished with potential cycling or pulsing above 1050 mV vs NHE. Once formed, the catalyst is stably adherent to the electrode surface, as the electrode coated with **BL** can be rinsed and transferred to a blank solution without any apparent loss of catalyst material. Polarizing the electrode to sufficiently high potential then results in oxygen evolution with essentially quantitative O₂ yield.[29] We previously found[18] that **BL** is stable for at least several hours at 1.4 V vs NHE; we can now extend this stability estimate to multiple days.

The **BL** samples used for the experiments described in this paper were generally prepared by the following method. **BL** was electrodeposited onto 1-cm² FTO-coated glass slides from a ca. 2 mM solution of complex **1** or **2** in potassium nitrate electrolyte for 2 h at 1.4 V. After this time, the layer is approximately 2 μm in thickness. SEM images of the layer (Figure 2, and Supporting Information) show the metal oxide surface features, including peaks and valleys that impart the appearance of a high apparent surface area to the material. Under the conditions of the microscopy, the layer appears to crack and expose the electrode's FTO-coated surface. In line with previous observations for hydrous iridium oxide films,[30,31] this cracking process likely results from dehydration due to the high vacuum required for the SEM imaging. This also seems likely because no activity is lost over many hours of use, suggesting that the cracking and fracturing process does not contribute under operating conditions. Cracking becomes more apparent as the slides are allowed to age because of dehydration under ambient conditions at longer times.[31]

There is a sufficient amount of material on the electrode surface in the case of the 2-μm thick layers to scrape it off with a razor blade and submit it for elemental analysis. We have previously published elemental analysis results on these 2-μm preparations of the **BL** immediately following deposition.[18]
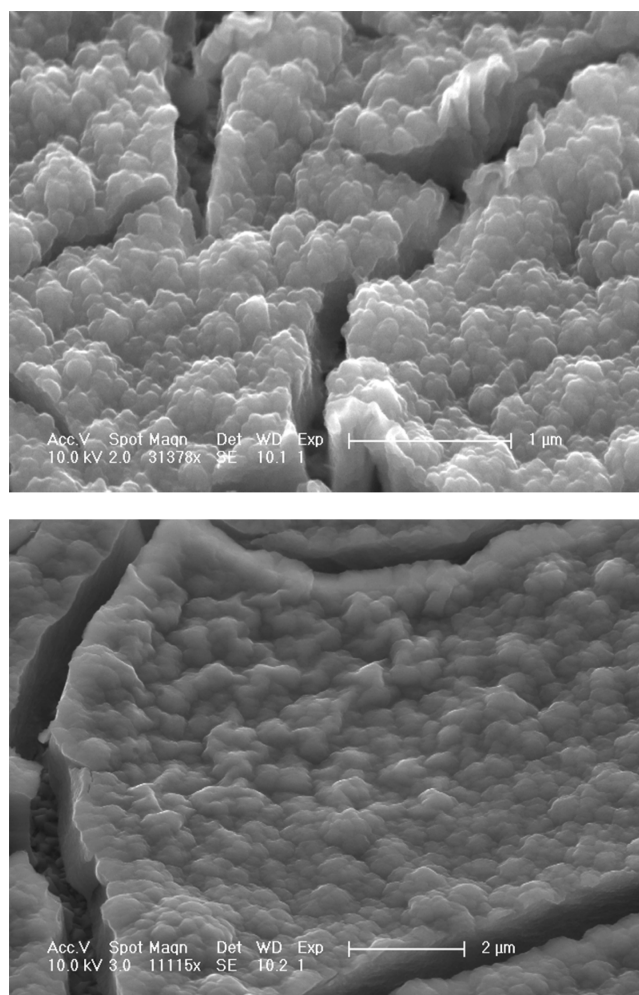
Figure 2. SEM images of **BL** after being deposited from a 3 mM solution of **1** at 1.4 V vs NHE for 2 h. The FTO coating on the electrode is visible through the crack on the left of the lower image.

After 2 h of deposition, **BL** is composed of iridium, oxygen, and approximately 10% carbon by mass.[32] This carbon content has its origin in the Cp* ligand, because no other sources of carbon are available under the deposition conditions.[33] The mass percent carbon in the precursor **1**, for example, is no greater than 23%. There is some uncertainty in this mass percent because of the unknown number of waters of crystallization in the isolated precursor material, but regardless it is far above the maximum measured for the initially deposited **BL** of about 10%. Importantly, this percent carbon by mass is less than half of the percent carbon by mass for the organometallic precursor, suggesting that significant ligand oxidation and carbon loss has occurred over the 2 h deposition. Additionally, the mass of **BL** nost likely includes water within the hydrous material.

We were interested in comparing both the activity of the catalyst and the carbon content versus time, as changes in either would indicate changes in the composition of the layer. We expected that the carbon content would likely decrease over time because of oxidation of the remnant carbon species from the precursor ligand, eventually converting the layer to a purely inorganic iridium oxide species. However, we find a nonzero carbon content even at very long times. To carry out this study, we prepared multiple identical FTO-glass electrodes with 2-μm layers of **BL** as described above; we then electrolyzed water at

1.4 V vs NHE for various increasing amounts of time with individual **BL** preparations. After the desired time had elapsed, we removed the slide from the electrolysis cell, allowed it to air-dry, and collected the catalyst for elemental analysis.

The results on the carbon content of the layer from this method are shown in the upper panel of Figure 3. The carbon
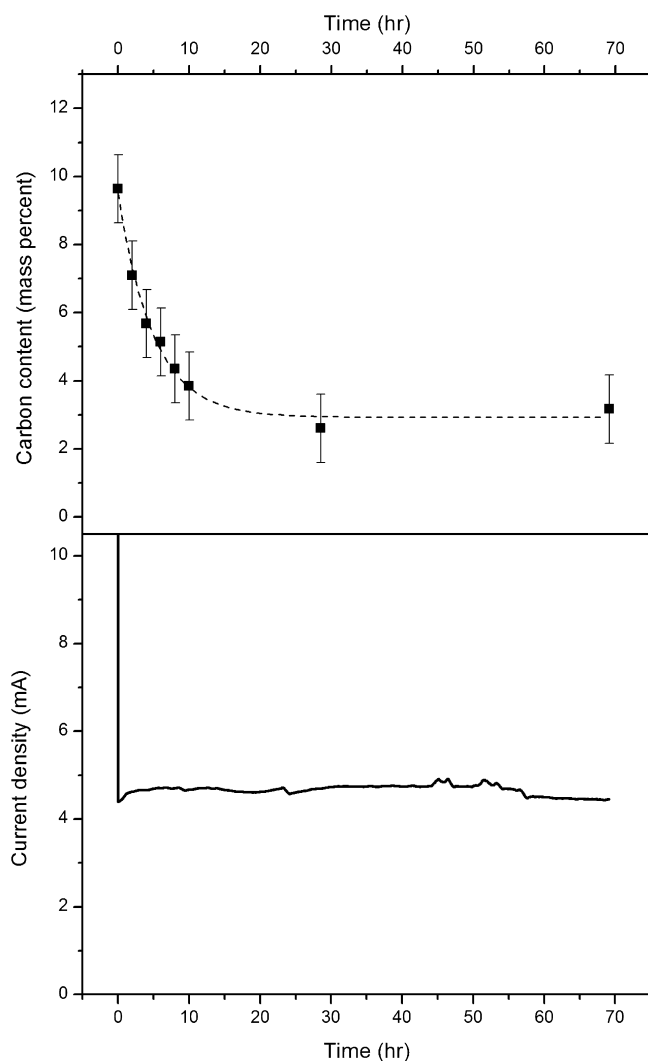
Figure 3. Carbon content (top panel) and catalytic activity measured as current per cm² (lower panel) as a function of time in hours. Dashed line in the top panel is fit with an exponential decay that asymptotically approaches 2.9 ± 0.2% carbon by mass.

content of the layer decreases over time starting from a maximum value after the initial deposition of around 10%. The behavior is asymptotic and approaches a nonzero value within the time window observed of 2.9 ± 0.2% carbon by mass. However, the mass percent carbon in **BL** at all times measured is less than the estimated carbon content of the precursor complexes. The nonzero asymptote may suggest that the carbon plays an unexpected role in the structure of the layer, rather than simply being an impurity imparted by the deposition process that eventually oxidizes away. However, contribution of surface-bound carbon species (including adventitious carbon, which may be a large contribution due to the high surface area of the material) versus any carbon content in the bulk subsurface material cannot be distinguished in this experiment.

We were next interested in looking at the activity of the catalyst over the same time period as the carbon content of the layer decreased asymptotically. The results are shown in the lower panel of Figure 3. Although the carbon content of **BL** is dropping, it is fully active without measurable loss in activity (measured as the steady-state current density) for at least 70 h. The activity, thus, does not change significantly as the carbon content drops; this strongly suggests that either (1) carbon is not bound in any form to the active site(s) of the catalysts or (2) it is bound in a highly modified form and as a low final percent of the catalyst mass. In either case, a majority of the original carbon in the layer is not connected directly with catalytic activity; the activity of the layer likely thus comes from iridium oxide material formed in situ from the organometallic precursor.

IR Spectroscopy. In our initial report on the formation and activity of **BL**,[18] we showed that the layer's carbon admixture could be probed with IR spectroscopy by scraping a layer off the electrode, making a pellet with potassium bromide, and collecting the IR spectrum. This spectrum showed the clear presence of C=O stretching frequencies in the region of 1300−1700 cm^{-1}, but not a significant signal for C−H stretching frequencies, which would be expected to appear around 2900 cm^{-1}. We, thus, concluded that the carbon admixture in the layer was an oxidized form of Cp* that contained C=O functional groups.

We have now extended this spectroscopic work to catalyst layers still on the electrode surface by use of diffuse reflectance infrared Fourier-transform spectroscopy (DRIFTS). With this technique, we are able to collect the infrared spectrum of **BL** directly without removing it from the electrode surface. This allows us to collect spectra before and after various periods of time that the film is subjected to water electrolysis conditions. Thus, we can monitor conversion of the carbon in the layer from its starting form to various other forms over the time of catalyst operation. Our study mirrors work on the oxidation of graphite electrodes and more recent work on graphene sheets under related harsh conditions, which results in the formation of graphitic oxide.[34]

When starting this study, we were interested in the possibility that **BL** might still show some C−H bonds on the surface after deposition from the soluble precursors. This would support our hypothesis that solution-phase oxidation of the precursor complexes results in the formation of insoluble aggregates that carry most or all of the carbon ligand onto the surface. Related work[35] in this area comes from Korzeniewski's group and co-workers; they have analyzed vibrational spectra relating to oxidation of organic molecules on electrode surfaces with relevance to fuel cell operation. Their studies have even tracked the fate of carbon with isotopic labeling. In our experiments, we attempted to observe C−H bonds at various thicknesses of the layer. The signals were obtained with layers that are fairly thin (deposited for 20 min at 1.4 V), and these are shown below in Figure 4.

As can be seen in Figure 4, a relatively thin **BL** shows stretching frequencies consistent with C−H bonds present in the material. However, upon electrolyzing water with **BL** at 1.4 V for as little as 15 min, the peak intensities have dropped markedly. After 30 min of electrolysis, there is only a slightly above background signal around 3000 cm^{-1}. After 45 min, the C−H stretching frequencies are completely indistinguishable from the background. Thus, the C−H bonds are oxidized under the conditions used here for water electrolysis. This is
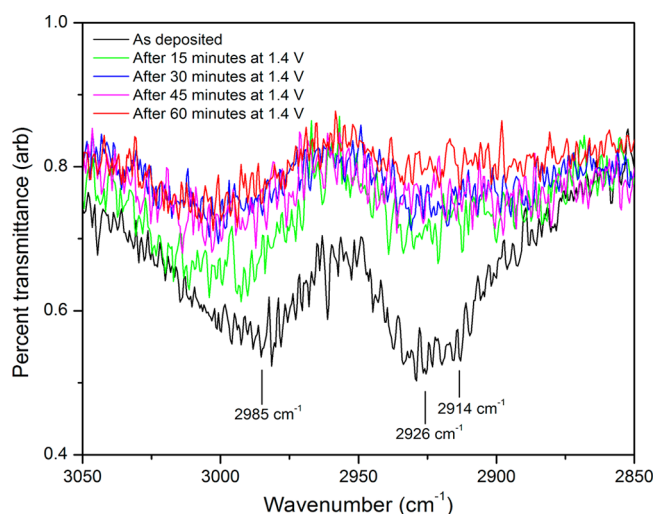
Figure 4. C−H stretching region of the infrared spectrum of one preparation of **BL** at various times of active water electrolysis. Black line: as-deposited **BL** from 20 min of deposition. Other lines: spectrum after subjecting **BL** to various times of water electrolysis at 1.4 V. H-bonding water contribution was subtracted from these data.

consistent with the loss of carbon from the layer, as observed in the elemental analyses, as well as our expectation that the benzylic C−H bonds of the Cp* ligand would be reactive under the highly oxidizing conditions.

Having observed that C−H bonds are present in the layer at short times, we next looked for interconversion of C=O frequencies over the same time scale. The IR spectra collected are shown in Figure 5. In the black trace of Figure 5, it is clear
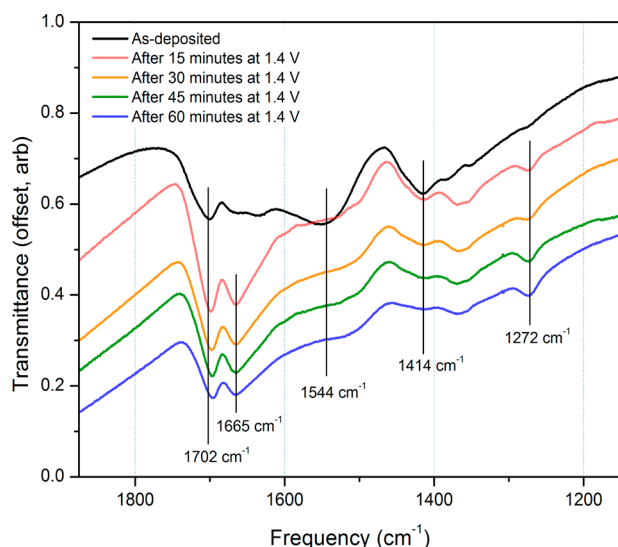
Figure 5. IR spectrum of **BL** in the C=O stretching region. Black line: **BL** as-deposited for 20 min at 1.4 V. Other lines: spectra of **BL** after water electrolysis for the indicated periods of time (15, 30, 45, and 60 min).

that there are frequencies consistent with C=O and C−O fragments already in the layer as-deposited after 20 min. There are three main features in this spectrum, centered at 1702, 1544, and 1414 cm^{-1}. Because the precursor complexes lack signals in this region, it is clear that already significant oxidative conversion has occurred on the Cp* ligand during the 20 min

deposition process. It is quite likely that most or all of the precursor Cp* ligand has been converted into a form that is no longer bound to iridium; a pentacarboxylated derivative of the cyclopentadiene ligand is known, but it is a poor ligand because of its low Lewis basicity.[36]

After water electrolysis for 15 min, further changes are apparent to the IR spectrum. The major peak at 1544 cm^{-1} present in the as-deposited film has now been lost. The peak at 1414 cm^{-1} has lost intensity as well. Furthermore, the peak at 1702 cm^{-1} has become more intense than in the as-deposited film. Additionally, new features have appeared at 1665 cm^{-1} and 1272 cm^{-1}. In the subsequent time points, these features become less intense versus the background, implying that the carbon content giving rise to these features is slowly being lost from the film. However, as stated above, the activity of the catalyst is not lost over this time period, which strongly suggests that the carbon being lost is not directly ligated to the active sites. Rather, it may be a component in the heterogeneous surface layer. Regardless, a small amount of carbon is found at long times in the layer, but much of the initial carbon is lost.

Electrochemistry of the Precursor and Catalyst Activity. As we have described previously, electrochemical oxidation of precursors **1** or **2** is completely irreversible on the time scale of electrochemical experiments, and leads to the formation of **BL** on the electrode surface. This is shown in Figure 6; the irreversible oxidation of the precursor dimer **2** onsets at approximately 1050 mV vs NHE. (Only the onset of the large, pseudocatalytic response is shown in Figure 6.) If the oxidation is cycled beyond about 1250 mV as shown in Figure 6, a new set of features centered at lower potentials becomes apparent; these are associated with the surface-bound, non-diffusional layer of **BL**, rather than the homogeneous precursor.[30] This irreversible behavior of **1** and **2** contrasts with the behavior of other iridium complexes, as most other iridium complexes do not deposit or form catalytic oxides. Here, we have used the reversible, one-electron oxidation of $[IrCl_6]^{3-}$ as a control case in the lower panel of Figure 6. Clearly, oxidation of this simple iridium compound does not result in formation of catalytic oxide. This is corroborated by extensive previous work on $[IrCl_6]^{3-}$.[37]

DFT calculations (see Supporting Information) confirm that the precursor dimer **2** can be oxidized at potentials relevant to those observed experimentally. However, at present, no oxidized intermediates could be isolated of relevance to the decomposition of **2**. Rapid precipitation of insoluble species may be related to oxo-bridge formation following oxidation of iridium (around 1.1−1.2 V vs NHE).

In a recent report, we have explored the catalytic activity of thin layers (in contrast to the thicker layers studied here) of various electrodeposited amorphous iridium oxide materials.[18,20,29] Using our electrochemical quartz crystal nanobalance technique, we found conditions under which surface loading of iridium material could be estimated for different precursors to the electrodeposited material. The conditions could then be manipulated to give roughly equivalent surface loadings of catalyst, thus enabling a reasonable comparison of activity. Among others, we compared electrodeposited materials formed from precursor **1**, a new related species $[CpIr(H_2O)_3]SO_4$, and iridium oxide from $[Ir(OH)_6]^{n+}$ as developed by Mallouk and co-workers.[8b] Under our conditions, the three materials were essentially indistinguishable in their overpotentials (measured at 0.5 mA cm^{-2}) and H-D kinetic isotope effects for water
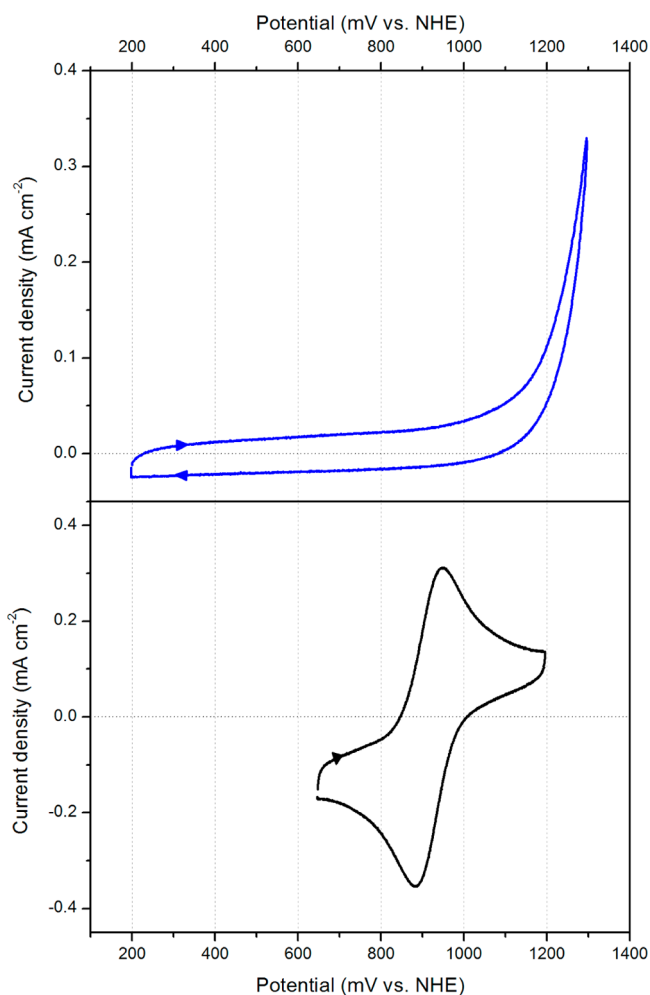
Figure 6. Single-cycle voltammetry for the dimer **2** (upper panel) and $[IrCl_6]^{3-}$ (lower panel). Conditions: $[Ir] = 10^{-3}$ M, scan rate: 100 mV/s, supporting electrolyte: 0.1 M KNO_3, basal-plane graphite working electrode. The redox change shown in the lower panel is the iridium(III/IV) couple (i.e., $[IrCl_6]^{3-}/[IrCl_6]^{2-}$).

oxidation. Thus, we concluded that the carbon content of **BL** does not play a large role in modulating catalytic activity over the time scale of the experiment. However, we did observe differences in deposition behavior and catalyst stability, motivating the current study. Moreover, estimating over-potentials with these highly active iridium materials can be challenging, because local pH gradients and bubble formation can be secondary influences on measurements of catalyst

activity.[29b] The amorphous materials are considerably more active than crystalline iridium oxide,[30] motivating a better understanding of their formation and use.

X-ray Absorption Spectroscopy (XAS). To gain more information about the structure of **BL** once it has formed, in situ XAS (including both XANES, X-ray absorption near edge structure, and XAFS, extended X-ray absorption fine structure) measurements were performed on the iridium films to determine their structure. XAS provides information on the local structure surrounding the absorbing metal center. To determine the oxidation state and local coordination geometry of the **BL** material, XAS measurements at the Ir-L_{III} edge were carried out. The oscillations in the XAFS spectrum are caused by interference patterns due to the outgoing and backscattered photoelectron waves originated from the X-ray absorbing atom and nearby scattering atoms. The Fourier transform of this interference pattern yields a pseudo radial distribution function centered on the iridium atoms, where the peaks correspond to specific atom−atom distances. By fitting a theoretically calculated spectrum based on a model structure to the experimental spectrum, local structural parameters around iridium atoms in the film can be extracted according to the following equation:[38]

$$\chi(k) = \sum_i \frac{F_i(k)S_0^2(k)N_i}{kR_i^2} \exp^{-2\sigma_i^2 k^2} \sin[2kR_i + \phi_i(k)]$$

where $F_i(k)$ is the backscattering amplitude, S_0 is the amplitude attenuation parameter, N_i is the coordination number, R_i is the distance from the Ir atom to its neighboring atoms, and σ_i is the Debye−Waller factor describing the divergence of the distances.

The layer was formed via electrochemical deposition at 1400 mV vs NHE, and then the electrode was held at a constant potential of 200 mV vs NHE in the presence of 0.1 M KNO_3 throughout the XAFS experiment to prevent film oxidation. The XAFS spectrum of the **BL** as prepared is shown in Figure 7. (The electrolyte for the data collection did not contain the precursor complex.) The spectrum in k-space was Fourier-transformed from $k = 3.7$ to $k = 10.5$, and the data were fit in R-space from $R = 1.2$ to $R = 3.2$. The first shell consists of 2 oxygen paths, with average lengths of 1.98 Å and 2.11 Å and coordination numbers of 3. Outside the first shell is a single Ir atom located 3.04 Å from the other Ir atom. The XAFS data indicate that the repeating units of these films are Ir "dimers", with the two Ir atoms connected by three bridging oxygens and with 3 terminal oxygen ligands on each Ir atom. It is interesting to note that the second shell shows no sign of the carbons from
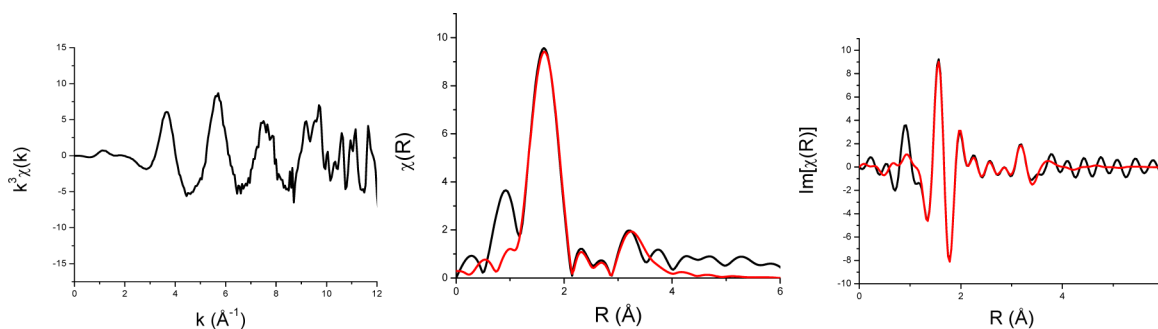
Figure 7. k-space (left panel), R-space (middle panel), and imaginary R-space (right panel) spectra of the **BL** material (black) and the fit (red); experiment performed in aqueous 0.1 M KNO_3 at 200 mV vs NHE on a graphite working electrode.

the methyl groups of the pentamethylcyclopentadienyl ligand, confirming that this ligand is not attached to iridium after the film is formed. There are also contributions from two oxygen or carbon atoms at a further distance of 3.81 Å away, which may correspond to the atoms of the ketomalonate groups proposed in a theoretical model described below.

X-ray Scattering Studies. The structure of **BL** across an extended distance range was examined by high energy X-ray scattering (HEXS) and pair density function analysis. The reduced pair distribution function, $G(r)$, is obtained by direct Fourier transform of HEXS data.[39] $G(r)$ is related to the atom pair electron density distribution, $\rho(r)$, by $G(r) = 4\pi[\rho(r) - \rho_o]$, where ρ_o is the average electron density.[40] HEXS patterns were measured across the reciprocal space scattering range 0.5 Å^{-1} to 24 Å^{-1} from ex situ aqueous slurries of **BL** scraped off of the electrode surface after different periods of electrolysis. Figure 8 shows $G(r)$ measured for a **BL** film deposited over 2 h
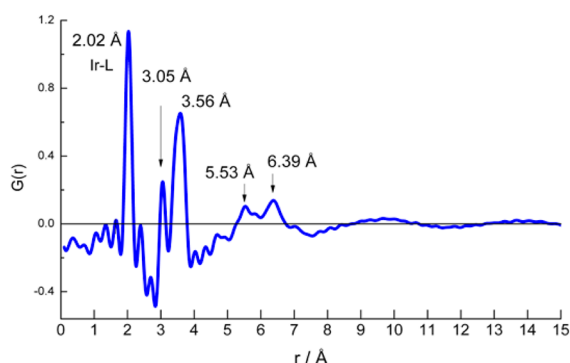

Figure 8. Reduced density pair function, $G(r)$, measured for **BL**. The sample was prepared ex situ as an aqueous slurry of **BL** material which was scraped off the FTO electrode surface.

of electrolysis (as described above). No differences were discerned between $G(r)$ measured for **BL** following 2 or 4 h of water electrolysis. The pattern shows a series of well-resolved correlation peaks that terminate at a distance of approximately 6.4 Å, with a partially resolved peak extending to 7.1 Å. The $G(r)$ data show that the amorphous **BL** lacks long-range order at distances beyond this range, but can be characterized by a pattern of discrete pair correlations at shorter distances.

The positions of the peaks at 2.02 Å and 3.05 Å correlate well with distances measured by XAFS, and can be identified with the first shell Ir-ligand atom distance and Ir−Ir distance for a multiple di- or tri-μ-(hydr)oxo-bridged dimer. A prominent peak is measured at 3.56 Å with broadened line shape indicative of multiple unresolved contributions. This feature possibly correlates with the 3.81 Å peak measured in the XAFS data. In addition, the HEXS-$G(r)$ shows inhomogeneously broadened features at longer distances, with peaks at 5.53 Å and 6.39 Å. We postulated that further guidance on interpretation of the $G(r)$ peaks would be obtained by comparison of these data for **BL** with $G(r)$ measured for precursors **1** and **2** in solution. Future work examining the thickness dependence of the XAFS and PDF data may provide further information as well, but was beyond the scope of the present study; the deposition time (cf. related results in Figure 3) could also have a large effect on the composition of the deposited material.

Panel A in Figure 9 shows the $G(r)$ measured for the $[(Cp*Ir)_2(OH)_3]OH$ dimer, **2**, in aqueous solution, and compared to $G(r)$ and $\rho(r)$ calculated from the crystal
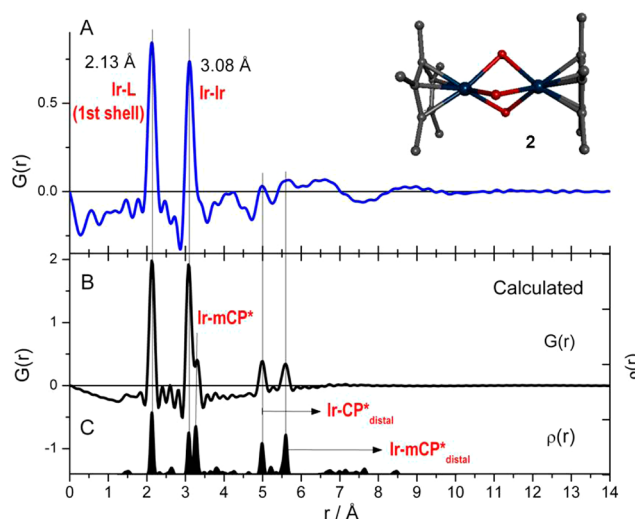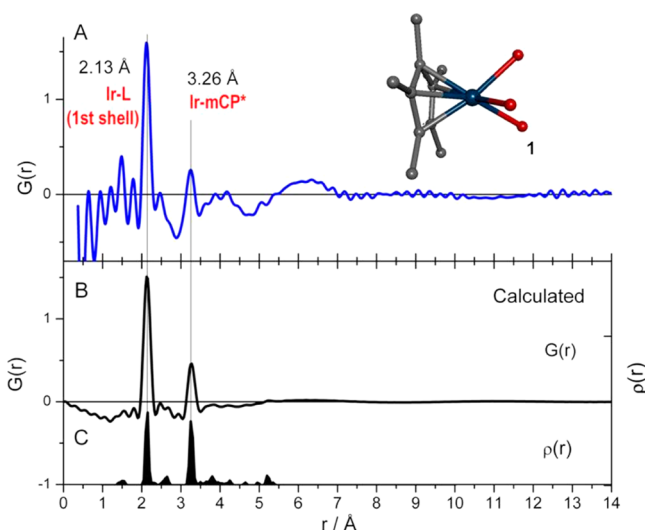

Figure 9. Panel A. Experimental $G(r)$ measured for the $[(Cp*Ir)_2(OH)_3]OH$, **2**, in aqueous solution. **Panel B.** $G(r)$ for **2** calculated from crystal coordinates. **Panel C.** The atomic pair distribution function, $\rho(r)$, calculated for **2** using a single Gaussian atomic form factor with a 0.3 Å^{-1} width.

coordinates, shown in Panels B and C, respectively. As described in the Methods, the calculated $G(r)$ used experimental atomic scattering factors[41] and solvent electron density, while the $\rho(r)$ was calculated using a single Gaussian form factor for all atoms to allow resolution of each of atom-pair peaks. The HEXS measurement shows good resolution of the Ir-ligand atom and Ir−Ir distances at 2.13 Å and 3.08 Å, respectively. These distances are slightly longer than comparable distances measured by XAFS and HEXS-$G(r)$ in **BL**. A notable feature of the experimental $G(r)$ pattern is the weakened contributions of the Ir−C correlations beyond the first coordination shell compared to those in the calculated patterns. This is particularly apparent for the Ir−C atom pair distances corresponding to the separation between the Ir and Cp* ligand, and the separations between Ir and methyl groups of the distal Cp* ligand. These are only poorly resolved at 5.0 Å and 5.6 Å in the experimental $G(r)$. The partial attenuation of the Ir-methyl-Cp* and Ir-Cp* distances in the calculated $G(r)$ compared to $\rho(r)$ arises from the use of exact atomic-specific scattering form factors and the electron density contrast with the solvent in the $G(r)$ calculation. In addition, the experimental $G(r)$ shows additional attenuation of these peaks. Modeling studies show this can be understood to arise from a higher disorder or thermal factor for the Cp* methyl groups, for example due to wagging motions.

Figure 10 shows the measured $G(r)$, and calculated $G(r)$ and $\rho(r)$, for the $[Cp*Ir(H_2O)_3]^+$ complex **1**. As expected, contributions in the range of 5−6 Å, corresponding to distal Cp* interactions, are absent in this compound, which is well-known to be a monomer in solution. Further, we note here that the attenuation of the Cp* methyl group contributions observed in the experimental $G(r)$ measured for **1** is likely due to thermal motion, as above. (A more detailed analysis of the solution phase $G(r)$ patterns will be presented elsewhere.)

Thus, overall, the measurements indicate key differences between the scattering patterns of **BL** versus the soluble precursor complexes **1** and **2**. The first-shell Ir-ligand atom distances suggest that the overall oxidation state of iridium in the ex situ film is higher than in the precursor complex. This

Figure 10. Panel A. Experimental $G(r)$ measured for $[Cp^*Ir(H_2O)_3]$, **1**, in aqueous solution. **Panel B**. $G(r)$ for **1** calculated from crystal coordinates. **Panel C**. The atomic pair distribution function, $\rho(r)$, calculated for **1** using a single Gaussian atomic form factor with a 0.3 $Å^{-1}$ width.

compares well with the blue color of the layer, which arises most likely from iridium(IV) centers. Further, comparing the Ir−Ir interactions in **BL** and complex **2**, longer-range Ir−C or Ir−O contributions are likely to contribute less prominently than Ir−Ir correlations, making direct conclusions about structure difficult. However, the $G(r)$ of **BL** appears to qualitatively contain some contribution from Cp* fragments as are found in **1** and **2**, which compares well to results from elemental analysis and DRIFTS as presented above. Regardless of this detail, **BL** is clearly distinct from the organometallic precursors **1** and **2**, and based on the changes to $G(r)$, η^5-Cp* is not expected to be bound to iridium.

Modeling of Proposed Components of the Layer. Computational modeling based on simulated annealing Monte Carlo (MC) and density functional theory (DFT) calculations in conjunction with simulations of X-ray absorption and X-ray scattering data were used to explore plausible structural models for **BL**. As proposed possible contributions, we found that a mixture of iridium ketomalonate substructures, **I** and **II** in Figure 11, could reproduce the pair-distance electron density distribution (PDF) and XAFS data. Notably, substructures **I** and **II** are plausible products of decomposition of the precursors **1** and **2**; short chain carboxylic acids are known
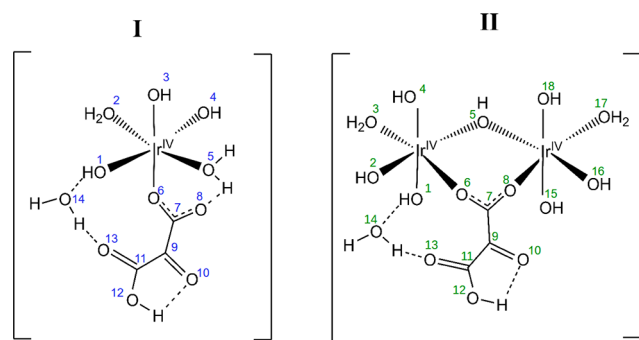
Figure 11. Schematic representations of **I** and **II**. They are composed of 9.3% and 5.6% carbon by mass, respectively.

decomposition products of aromatics in electrochemical oxidations with iridium materials,[42] and organic ketoacids are produced upon oxidation of humic acid.[43] Glycerol is also readily converted to ketomalonic acid (also known as oxomalonic acid, mesoxalic acid, or oxopropanedioic acid) under oxidizing conditions.[44] It is, thus, possible that ketomalonic acid, having more chelation modes and possible sites for hydrogen bonding, could be retained in **BL**. Appealingly, substructures **I** and **II** are dominated by iridium and oxygen in their composition, and thus would be predicted to give elemental analysis data consistent with that found for **BL**. Specifically, the substructures analyze to mass percentages of carbon of 9.3% and 5.6%, respectively for **I** and **II**; these compare well with the carbon content of **BL**, which has between 10% and 3% carbon by mass, depending on the point at which the analysis is carried out. We were interested in substructures **I** and **II** as possible components of **BL**, which would be present in addition to domains of iridium oxide.

Figure 12 shows the calculated isotropic XAFS and PDF spectra for the MC-refined structures of **I** and **II**, together with
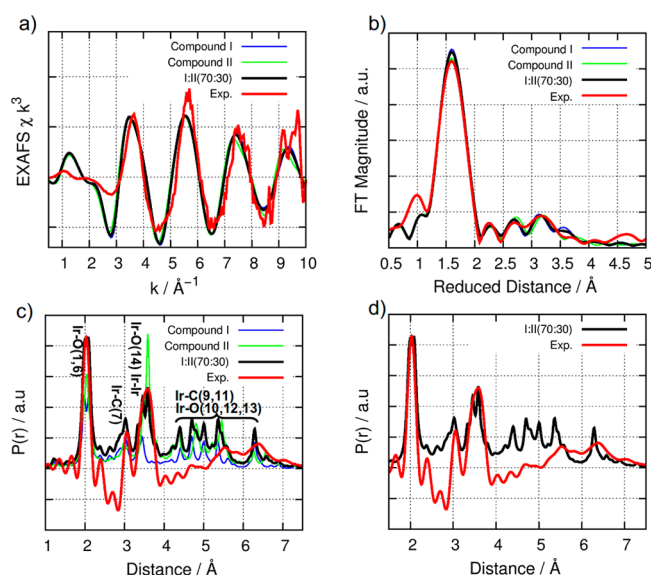
Figure 12. Comparisons between experimental isotropic XAFS (upper panels) and PDF (lower panels) spectra of the **BL** (red line) and calculated spectra of **I** (blue line), **II** (green line), and a mixture of the two substructures in a 70:30 ratio (black line). Panels A and B: isotropic k^3-weighted XAFS data in the momentum (k) space (panel A) and Fourier transform of $\chi(k)$ (panel B). Panels C and D: simulated and experimental PDF spectra. Assigned pair atom distances are shown on top of the corresponding PDF peaks. The width of the Lorentzian function used for the calculated PDF is 0.1 Å. (XAFS and PDF for the MC refined and optimized structures of substructures **I** and **II** are also shown in the Supporting Information.).

the experimental data for **BL**. Computational models of **I** and **II** were obtained using geometry optimization at the DFT/B3LYP level followed by MC refinement with respect to XAFS spectra, as described in the method section. Calculated XAFS spectra for the refined DFT-models of both **I** and **II** are in good agreement with isotropic Ir-L$_{III}$-edge XAFS experimental spectra. Comparison between the experimental PDF spectrum of **BL** and calculated PDF spectra of the refined DFT models of **I** and **II** is shown in Figure 12, Panel C. The positions and relative intensities of experimental PDF peaks at 2.03 and 3.06 Å are reproduced in the calculated spectra of both iridium

substructures, corresponding to first shell Ir−O (1−6) distances and second shell Ir−C (7) distance of the ketomalonate carboxylate group, respectively (see numbering in Figure 11). Similarity between the experimental PDF peak at 3.56 Å and simulated spectra of the refined DFT models of **I** and **II** can be obtained considering a mixture of the substructures with a 70:30 ratio, as in Figure 12, Panel D. The peak at 3.56 Å is reproduced by considering the Ir−Ir distance connected through a protonated μ-oxo bridge in substructure **II**; however, a further water hydration shell surrounding the octahedral iridium center of substructure **I** cannot be discounted (see Supporting Information). A series of peaks present in the 4−7 Å region of the calculated spectra is associated with the tail of the ketomalonate ligand of both monomeric and dimeric species, involving the Ir−C(9,11) and Ir−O(10,12,13) distances. The inhomogeneous broadening observed in this region of the experimental PDF spectrum of **BL** may be explained by considering different conformations of the ketomalonic acid tail that would be accessible by thermal fluctuations.

In the proposed mixture, substructures **I** and **II** could be linked by μ-oxo or μ-hydroxo bridges, or extended hydrogen-bonding networks involving hydroxyl groups and water ligands, giving rise to the extended amorphous structure of **BL**. This would give a material not unlike the "gel-like" hydrous iridium(III,IV) oxides which can be prepared by electrochemical cycling of iridium metal.[45] Some sputtered iridium oxides have also been reported to form "fractal structures" which might be obscured in our electrodeposited material.[46] Certainly, because our material is composed of domains of iridium oxide as shown in the XAFS and HEXS results, behavior similar to amorphous, hydrous iridium(III/IV) oxide is not surprising.

The constituents of the proposed carbon-containing fragment are also chemically sensible, although we have not detected them directly. The ketomalonate ligand could form upon oxidation of the Cp* ligand and may be stable under highly oxidizing conditions, especially in the heterogeneous environment of the electrode surface. Analogous dicarboxylic acid ligands, such as malonate, have been previously used as capping agents to stabilize highly active IrO$_2$ nanoparticles.[47] To the best of our knowledge, the structure of malonate has not been confirmed in the assembled nanoparticles, suggesting that it may be oxidized to another form, like ketomalonate in situ. Ketomalonic acid has also proven to be an effective bridging ligand for multinuclear metal complexes, such as [Cu$_3$(Hmesox)$_3$]$^{3-}$.[48] The proposed fragment is also consistent with IR spectroscopy of the layer that shows loss of C−H vibrational frequencies upon water electrolysis, because neither **I** nor **II** have C−H bonds. Further work (see Supporting Information) on modeling the IR spectra of substructures **I** and **II** suggests reasonable agreement between the actual IR spectra of **BL** and the calculated IR spectra of the hypothetical substructures. At present, all efforts to isolate the organic components within **BL** have been unsuccessful, perhaps as a result of the stability of iridium oxide materials to all but the harshest chemical treatments.

■ DISCUSSION

Our original observation of the electrodeposition of **BL** from homogeneous solutions containing complexes **1** or **2** came as a surprise to us.[20] To date, we know of no other case where a well-defined organometallic precursor has been shown to be useful for the electrodeposition of a highly active water-oxidation catalyst. Related electrodepositions have been studied from simple inorganic salts of transition metals such as cobalt, nickel, and manganese.[49] Indeed, electrodeposition of water-oxidation catalysts has emerged as a promising method for developing new materials in this area. One emerging trend from current work suggests that the deposition method and conditions have a strong effect on the activity of the electrodeposited material. Consequently, we have been eager to investigate the properties of our electrodeposited iridium **BL** material, because the use of a molecular organometallic species as the catalyst precursor opens the possibility of affecting the structure and morphology of the heterogeneous catalyst material.[29] Furthermore, the ambiguity of homogeneous and heterogeneous water-oxidation catalysis encouraged us to investigate this unique example of a molecular organometallic compound converting to a secondary metal oxide material upon oxidation.

From the elemental analysis data, it is clear that **BL** is essentially an amorphous iridium oxide material. The carbon content quickly diminishes, reaching a small limiting value over hours of water electrolysis. During this time, the electrocatalytic activity is not lost, suggesting that a majority of the carbon in the layer (which arises from the organometallic precursor) is not required for highest activity. Notably, however, distinguishing activity of species bearing carbonaceous ligands from purely inorganic iridium oxide will be rather difficult, since all the species are expected to have high activity. The carbon content in the layer after prolonged electrolysis completely lacks C−H bonds and is dominated (in the IR spectra, at least) by C=O and C−O fragments; these observations are consistent with the highly oxidizing conditions of catalyst operation which presumably drive loss of carbon and formation of iridium oxide.

The XAS, XAFS, and HEXS data confirmed our hypothesis that the structure of the deposited material is markedly different from the precursor complexes. Thus, even though the film arises initially from oxidation of the organometallic precursor (a process involving oxidation events and perhaps deprotonation of iridium-bound water or hydroxide), the film itself does not contain a significant fraction of iridium bound to η^5-Cp*. In fact, modeling of the scattering data suggests that the deposited **BL** is a completely amorphous iridium oxide material with a small domain size of <7 Å. This small domain size likely contributes to the observed high activity, because high surface area presents more active sites for catalyst function. This is further consistent with our observation that the amorphous material is much more active than crystalline iridium dioxide.[29]

However, the layer contains carbon in significant quantity at short times; we have modeled this carbon here as a ketomalonate-containing fragment which is consistent with the spectroscopic results. Certainly, the notion of a carbonaceous species that is bound to iridium in the heterogeneous material is surprising, because the conditions are highly oxidizing. However, malonate is known to stabilize highly active iridium oxide nanoparticles.[47] We propose the substructures **I** and **II** as *possible* constituents of **BL**, along with the major components of hydrous iridium(III,IV) oxides and amorphous iridium(IV) oxide. The electrochemical properties of fresh **BL** are distinct from all previously studied iridium-oxide layers, but because crystalline iridium(IV) oxide is electrochemically silent up to oxygen-evolving potentials,[29] we cannot strictly distinguish contributions from the inorganic material, despite lack of any apparent long-range order in X-ray

scattering or powder X-ray diffraction. To the best of our knowledge, there has also been little work examining interconversion of various forms of iridium oxide.

Regardless of the state of the carbon in the deposited material, oxidation of the organometallic precursors leads to the formation of the catalyst. **BL** itself is mechanically stable and no loss of material from the anode surface is apparent over hours of continuous use. The carbon may help play a structural role by bridging between smaller domains in the overall amorphous material, but taken together, the data show **BL** is an amorphous iridium oxide material. The small domain size of the iridium oxide likely thus contributes to the high catalyst activity.

■ CONCLUSIONS

A combined experimental-theoretical study has examined **BL**, a highly active and amorphous iridium oxide electrocatalyst for water oxidation. **BL** is electrodeposited from organometallic precursors. Electrochemical methods, IR spectroscopy, elemental analysis, and synchrotron X-ray methods confirm that **BL** is significantly different in structure from its organometallic precursors, an observation consistent with the highly oxidizing conditions under which **BL** forms. Specifically, there are changes in the X-ray scattering patterns upon formation of the heterogeneous material, as well as changes in the first coordination shell as measured by XAFS. Computational modeling suggests ketomalonate as a possible component of the remaining carbon in the layer. Because **BL** has among the lowest measured overpotentials for water oxidation currently known (ca. 200 mV at 0.5 mA cm^{-2} at pH 3), future work will continue examination of the mechanism(s) of **BL** formation, as well as parallel work aimed at improving the activity and longevity of homogeneous water-oxidation catalysts.

■ EXPERIMENTAL SECTION

General Procedures. Complexes **1** and **2** were synthesized as previously reported.[50] Aqueous solutions were prepared with 18.2 MΩ cm Milli-Q water.

Infrared spectra were collected on a Nicolet 6700 FT-IR spectrometer equipped with a Smart Collector DRIFTS (diffuse reflectance) accessory. The spectra of thin layers of **BL** were obtained with a custom sample holder that was machined to accommodate the FTO-coated glass (Hartford Glass Co., Hartford City, Indiana) electrodes. Samples were rinsed with copious amount of deionized water and allowed to dry at room temperature before the spectra were collected.

Scanning electron microscopy (SEM) images were obtained with an FEI ESEM XL-30 system. Images were normally collected within 5 h of sample preparation. The acceleration voltage was 10 keV. Additional SEM micrographs (see Supporting Information) and elemental analysis data were collected on a JEOL JSM-IC848A scanning electron microscope equipped with an iXRF EDS-2000 X-ray energy dispersive spectrometer (Instrumental conditions: acceleration voltage 20 kV, and working distance, 17−20 mm).

Voltammetry. The measurements were made on a Princeton Applied Research Versastat 4-400 or model 273 potentiostat/galvanostat using a standard three-electrode configuration. FTO-coated glass or a graphite rod served as the working electrode, as described in the main text. A platinum wire was used as the counter electrode, and a Ag/AgCl electrode (Bioanalytical Systems, Inc.) was used as the reference (Ag/AgCl vs NHE: +197 mV). Experiments were carried out in unbuffered solutions containing 0.1 M KNO$_3$ (Strem Chemicals) as the supporting electrolyte. The solution pH was adjusted with dilute potassium hydroxide or nitric acid in some experiments, as noted.

X-ray Absorption Spectroscopy (XAS). The iridium L-edge X-ray absorption near edge structure (XANES) and X-ray absorption fine

structure (XAFS) were collected at beamline 12BM at the Advanced Photon Source of Argonne National Laboratory. Si(111) double crystals were used in the monochromator. Two mM solutions of complex **1** or **2** in aqueous 0.1 M KNO$_3$ solution were used to electrochemically form **BL**. Approximately 10 mL of the iridium solution was placed into a kapton-windowed cell with a graphite rod as the working electrode, a Pt wire as the auxiliary electrode, and Ag/AgCl as the reference electrode. A potentiostat was set at 1.4 V for 2 h to deposit a layer of approximately 2-μm thickness. Following the electrodeposition, the remaining solution was then removed and replaced with ∼10 mL of the 0.1 M KNO$_3$ solution. The X-rays were focused onto the layer deposited on the graphite electrode, and the absorption was detected in fluorescence mode using a Canberra 13-element germanium solid state detector, which was set to collect the Kα emission line of Ir. XAFS data analysis was performed with the Athena and Artemis packages based on IFEFFIT and FEFF programs.[51,52] Theoretical models were constructed with the program FEFF and were fit to the experimental data using Artemis.

HEXS and PDF Analyses. High energy X-ray scattering patterns (HEXS) were measured at beamline 11-ID-B at the Advanced Photon Source of Argonne National Laboratory using an incident X-ray energy of 60 keV.[53] The sample scattering patterns were corrected for solvent, container, and instrument background scattering, and then for multiple scattering, X-ray polarization, sample absorption, and Compton scattering using the program PDFgetX2[39b] to yield the reduced scattering structure function $S(q)$. Direct Fourier transform of $S(q)$:

$$G(r) = \frac{2}{\pi} \int_0^{q_{max}} q[S(q) - 1] \sin(qr) \, dq \tag{1}$$

with q_{min} extrapolated to 0 below q = 0.7 Å^{-1} and using q_{max} = 24 Å^{-1} gave the experimental pair distribution function shown in the main text $G(r) = 4\pi r[\rho(r) - \rho_o]$, where $\rho(r)$ is the atomic pair electron density function and ρ_o is the average electron density.[39c] $G(r)$ calculated from coordinate models for the Cp*Ir precursor complexes were calculated using methods described previously.[19c]

Computational Methods. All electronic structure calculations were performed using the Jaguar electronic structure program[54] and the B3LYP exchange-correlation functional with unrestricted Kohn−Sham wave functions (UB3LYP).[55,56]

For modeling of the XAFS and X-ray scattering data, all minimum energy configurations involve low-spin d^5 Ir(IV) centers (i.e., $S = \frac{1}{2}$ for each metal center). The ground-state electronic configuration of the dimeric species (substructure **II**) was obtained in a broken symmetry (BS) state,[57] where the α and β electronic densities are localized on different metal centers with antiferromagnetic coupling. A mixed basis set was employed, including the LACVP basis set to account for a relativistic description of electron−core potentials (ECPs) for the Ir(IV) centers and the 6-311G* basis set[58] for the rest of the atoms.

Simulated Annealing Monte Carlo (MC) Method. Computational models of substructures **I** and **II** that match experimental isotropic XAFS data of **BL** were obtained by refining the structures of the optimized DFT models. This was achieved by minimizing a cost function based on the sum of the square deviations between the experimental and calculated XAFS spectra. The cost function minimization has been performed employing a Monte Carlo (MC) method. In MC optimization steps, all atoms are allowed to move, excluding the ketomalonic acid tail (atoms 9−13), according to the Metropolis algorithm. Hydrogen atoms were not taken into account in the refinement procedure because their presence minimally affects the simulated XAFS. The probability of accepting a new atomic position is given by $p = min[1, \exp(-\Delta F/k_B T)]$, with ΔF denoting the total cost function difference between the final and the initial state. We have performed 10 annealing steps for each model compound, with temperature T being varied from 100 to 0 K, and with a temperature decay of 0.2/step for building the initial models. Further MC refinements of optimized DFT structures were performed at 0 K.

X-ray Diffraction Spectra Simulations. The intensity of the radial diffraction pattern is related to the Fourier transform of the pair correlation function $P(\mathbf{r})$ of the scattering elements[59] according to

$I(q) = 4\pi \int P(\mathbf{r})(\sin(q\mathbf{r})/q\mathbf{r}) \, d\mathbf{r}$, where $P(\mathbf{r})$ is a function in the real space that gives the probability of finding a scattering element at distance $\mathbf{r}$ from another situated at $\mathbf{r} = 0$, and q is the momentum space variable. In the case of X-ray diffraction, electron clouds around atoms act as scattering elements that are responsible for diffraction.[60] We have calculated an approximated pair-distance electron density distribution $P(\mathbf{r})$ that can be directly compared with Fourier transformed experimental diffraction patterns. In our calculations, atomic form factors are approximated by Lorentzian functions of arbitrary width, centered at the position of the scattering species. The resulting approximated pair-distance electron density distribution function is, thus, $P(\mathbf{r}) = 1/N_p \sum Z_m Z_n I_{mn}(\mathbf{r})$, where Z_m and Z_n are the atomic numbers of scattering centers m and n, respectively, I_{mn} is an arbitrary narrow electron density distribution with a Lorentzian distribution centered at $\mathbf{r} = \mathbf{r}_{mn}$, and N_p is a normalization constant. A width of 0.1 Å has been used for the Lorentzian functions.

XAFS Simulations. Isotropic Ir L_3-edge XAFS spectra of substructures **I** and **II** were calculated using the ab initio real space Green function approach as implemented in the FEFF code (version 8.30).[61] The experimental XAFS data $\chi(E)$, that is, the fractional change in absorption coefficient of Ir atoms induced by neighboring atoms, are converted into momentum (k) space using the transformation $k = [(2m_e/(h/2\pi)^2)(E - E_0)]^{1/2}$, where m_e is the mass of the electron and h is the Planck's constant. The calculated XAFS data are obtained by fitting the energy of the absorption edge (E_0) and the Debye–Waller factors (DWF, σ) against the experimental $\chi(k)$, using the IFEFFIT code.[52] For the refined DFT-models of substructures **I** and **II**, we obtained fitted E_0 values of 11198.8 and 11199.5 eV, respectively, and fitted DWF equal to 0.00094 and 0.0021 Å^{-2}, respectively. DW factors are considered to be the same for all the calculated interference paths, that is, the two and three legs paths. A fractional cosine-square (Hanning) window with $\Delta k = 1$ was applied to the experimental and calculated XAFS data. A grid of k points equally spaced at 0.05 Å^{-1} was used for the Fourier transformation (FT) of $\chi(k)$ in the k range 1–10 Å^{-1}.

ASSOCIATED CONTENT

Ⓢ Supporting Information

Additional SEM images, additional results and details from the computational modeling, and atomic coordinates for calculated structures. This material is available free of charge via the Internet at http://pubs.acs.org.

AUTHOR INFORMATION

Corresponding Author

*E-mail: gary.brudvig@yale.edu (G.W.B.), robert.crabtree@yale.edu (R.H.C.), victor.batista@yale.edu (V.S.B.), tiede@anl.gov (D.M.T.), chen@anl.gov (L.X.C.).

Present Addresses

[†]Beckman Institute, and Division of Chemistry and Chemical Engineering, California Institute of Technology, MC 139-74, Pasadena, California 91125, United States.

[⊗]Dipartimento di Chimica "G. Ciamician", Università di Bologna, V. F. Selmi 2, 40126 Bologna, Italy.

Notes

The authors declare no competing financial interest.

ACKNOWLEDGMENTS

REFERENCES

(1) (a) Bockris, J. O. M. *Energy: The Solar-Hydrogen Alternative*; Hogbin and Poole: Redfern, Australia, 1975. (b) Bard, A. J.; Fox, M. A. *Acc. Chem. Res.* **1995**, *28*, 141. (c) Meyer, T. J. *Acc. Chem. Res.* **1989**, *22*, 163. (d) McKone, J. R.; Warren, E. L.; Bierman, M. J.; Boettcher, S. W.; Brunschwig, B. S.; Lewis, N. S.; Gray, H. B. *Energy Environ. Sci.* **2011**, *4*, 3573.

(2) Pourbaix, M. *Atlas of Electrochemical Equilibria in Aqueous Solutions*; Pergamon Press: Oxford, U.K., 1966.

(3) (a) Beer, H. B. *J. Electrochem. Soc.* **1980**, *127*, 303C. (b) Hayfield, P. C. S. *Platinum Met. Rev.* **1998**, *42*, 116.

(4) (a) Millet, P.; Durand, R.; Pineri, M. *Int. J. Hydrogen Energy* **1990**, *15*, 245. (b) Millet, P.; Andolfatto, F.; Durand, R. *Int. J. Hydrogen Energy* **1996**, *21*, 87. (c) Smith, W. *J. Power Sources* **2000**, *86*, 74.

(5) Comninellis, C.; Vercesi, G. P. *J. Appl. Electrochem.* **1991**, *21*, 136.

(6) Wöhler, L.; Witzmann, W. *Z. Anorg. Chem.* **1908**, *57*, 323.

(7) (a) Nakagawa, T.; Beasley, C. A.; Murray, R. W. *J. Phys. Chem. C* **2009**, *113*, 12958–12961. (b) Nakagawa, T.; Bjorge, N. S.; Murray, R. W. *J. Am. Chem. Soc.* **2009**, *131*, 15578–15579.

(8) (a) Zhao, Y.; Hernandez-Pagan, E. A.; Vargas-Barbosa, N. M.; Dysart, J. L.; Mallouk, T. E. *J. Phys. Chem. Lett.* **2011**, *2*, 402–406. (b) Zhao, Y.; Vargas-Barbosa, N. M.; Hernandez-Pagan, E. A.; Mallouk, T. E. *Small* **2011**, *7*, 2087–2093.

(9) (a) Hara, M.; Waraksa, C. C.; Lean, J. T.; Lewis, B. A.; Mallouk, T. E. *J. Phys. Chem. A* **2000**, *104*, 5275–5280. (b) Morris, N. D.; Suzuki, M.; Mallouk, T. E. *J. Phys. Chem. A* **2004**, *108*, 9115–9119. (c) Hoertz, P. G.; Kim, Y.-I.; Youngblood, W. J.; Mallouk, T. E. *J. Phys. Chem. B* **2007**, *111*, 6845–6856.

(10) Youngblood, W. J.; Lee, S.-H. A.; Kobayashi, Y.; Hernandez-Pagan, E. A.; Hoertz, P. G.; Moore, T. A.; Moore, A. L.; Gust, D.; Mallouk, T. E. *J. Am. Chem. Soc.* **2009**, *131*, 926–927.

(11) (a) Stonehart, P.; Kozlowska, H. A.; Conway, B. E. *Proc. R. Soc. London A* **1969**, *310*, 541–563. (b) Rand, D. A. J.; Woods, R. *J. Electroanal. Chem. Interfacial Electrochem.* **1974**, *55*, 375–381. (c) Capon, A.; Parsons, R. *J. Electroanal. Chem. Interfacial Electrochem.* **1972**, *39*, 275–286. (d) Buckley, D. N.; Burke, L. D. *J. Chem. Soc., Faraday Trans. 1* **1975**, *71*, 1447–1459. (e) Pickup, P. G.; Birss, V. I. *J. Electroanal. Chem. Interfacial Electrochem.* **1987**, *220*, 83–100.

(12) Gottesfeld, S.; Srinivasan, S. *J. Electroanal. Chem. Interfacial Electrochem.* **1978**, *86*, 89–104.

(13) (a) Beni, G.; Schiavone, L. M.; Shay, J. L.; Dautremont-Smith, W. C.; Schneider, B. S. *Nature* **1979**, *282*, 281–283. (b) Khakani, M. A.; Chaker, M.; Gat, E. *Appl. Phys. Lett.* **1996**, *69*, 2027–2029.

(14) Gottesfeld, S.; McIntyre, J. D. E.; Beni, G.; Shay, J. L. *Appl. Phys. Lett.* **1978**, *33*, 208–210.

(15) Conway, B. E.; Mozota, J. *Electrochim. Acta* **1983**, *28*, 9–16.

(16) McDaniel, N. D.; Coughlin, F. J.; Tinker, L. L.; Bernhard, S. *J. Am. Chem. Soc.* **2007**, *130*, 210–217.

(17) (a) Blakemore, J. D.; Schley, N. D.; Balcells, D.; Hull, J. F.; Olack, G. W.; Incarvito, C. D.; Eisenstein, O.; Brudvig, G. W.; Crabtree, R. H. *J. Am. Chem. Soc.* **2010**, *132*, 16017–16029. (b) Hull, J.

1870

dx.doi.org/10.1021/ic301968j | *Inorg. Chem.* 2013, 52, 1860–1871

F.; Balcells, D.; Blakemore, J. D.; Incarvito, C. D.; Eisenstein, O.; Brudvig, G. W.; Crabtree, R. H. *J. Am. Chem. Soc.* **2009**, *131*, 8730−8731. (c) Brewster, T. P.; Blakemore, J. D.; Schley, N. D.; Incarvito, C. D.; Hazari, N.; Brudvig, G. W.; Crabtree, R. H. *Organometallics* **2011**, *30*, 965−973.

(18) Blakemore, J. D.; Schley, N. D.; Olack, G. W.; Incarvito, C. D.; Brudvig, G. W.; Crabtree, R. H. *Chem. Sci.* **2011**, *2*, 94−98.

(19) (a) Crabtree, R. *Acc. Chem. Res.* **1979**, *12*, 331−337. (b) Anton, D. R.; Crabtree, R. H. *Organometallics* **1983**, *2*, 855−859. (c) Crabtree, R. H.; Mihelcic, J. M.; Quirk, J. M. *J. Am. Chem. Soc.* **1979**, *101*, 7738−7740. (d) Crabtree, R. H.; Mellea, M. F.; Mihelcic, J. M.; Quirk, J. M. *J. Am. Chem. Soc.* **1982**, *104*, 107−113.

(20) Schley, N. D.; Blakemore, J. D.; Subbaiyan, N. K.; Incarvito, C. D.; D'Souza, F.; Crabtree, R. H.; Brudvig, G. W. *J. Am. Chem. Soc.* **2011**, *133*, 10473−10481.

(21) (a) Related experiments dealing with chemically-driven water oxidation have provided similar data. Specifically, oxidation of **2** has been shown by dynamic light scattering to result in particle formation, whereas other half-sandwich iridium complexes do not decompose to form particles. (b) Hintermair, U.; Hashmi, S. M.; Elimelech, M.; Crabtree, R. H. *J. Am. Chem. Soc.* **2012**, *134*, 9785−9795.

(22) (a) Savini, A.; Belanzoni, P.; Bellachioma, G.; Zuccaccia, C.; Zuccaccia, D.; Macchioni, A. *Green Chem.* **2011**, *13*, 3360−3374. (b) Zuccaccia, C.; Bellachioma, G.; Bolano, S.; Rocchigiani, L.; Savini, A.; Macchioni, A. *Eur. J. Inorg. Chem.* **2012**, *2012*, 1462−1468.

(23) Park-Gehrke, L. S.; Freudenthal, J.; Kaminsky, W.; DiPasquale, A. G.; Mayer, J. M. *Dalton Trans.* **2009**, 1972−1983.

(24) Wang, C.; Wang, J.-L.; Lin, W. *J. Am. Chem. Soc.* **2012**, *134*, 19895−19908.

(25) Lee, P. A.; Citrin, P. H.; Eisenberger, P.; Kincaid, B. M. *Rev. Mod. Phys.* **1981**, *53*, 769−806.

(26) Reimann, S.; Stotzel, J.; Frahm, R.; Kleist, W.; Grunwaldt, J.-D.; Baiker, A. *J. Am. Chem. Soc.* **2011**, *133*, 3921−3930.

(27) Sayers, D. E.; Stern, E. A.; Lytle, F. *Phys. Rev. Lett.* **1971**, *27*, 1204−1207.

(28) Westre, T. E.; Kennepohl, P.; DeWitt, J. G.; Hedman, B.; Hodgson, K. O.; Solomon, E. I. *J. Am. Chem. Soc.* **1997**, *119*, 6297−6314.

(29) (a) Blakemore, J. D.; Schley, N. D.; Kushner-Lenhoff, M. N.; Winter, A. M.; D'Souza, F.; Crabtree, R. H.; Brudvig, G. W. *Inorg. Chem.* **2012**, *51*, 7749−7763. (b) Kushner-Lenhoff, M. N.; Blakemore, J. D.; Schley, N. D.; Crabtree, R. H.; Brudvig, G. W. *Dalton Trans.* **2013**, DOI: 10.1039/C2DT32326E

(30) Birss, V.; Myers, R.; Angerstein-Kozlowska, H.; Conway, B. E. *J. Electrochem. Soc.* **1984**, *131*, 1502−1510.

(31) Conway, B. E.; Mozota, J. *Electrochim. Acta* **1983**, *28*, 9−16.

(32) As reported previously, elemental analyses of **BL** do not sum to 100%. This is likely due to incomplete conversion of the iridium material, which is well-known to be an issue with iridium oxide materials.

(33) Ambient atmospheric carbon dioxide gas or dissolved bicarbonate are also plausible sources of carbon. However, iridium oxides are not known to uptake carbon dioxide in this way. Furthermore, we form the catalyst under strongly oxidizing and acidic conditions.

(34) (a) Swain, G. M. *J. Electrochem. Soc.* **1994**, *141*, 3382−3393. (b) Lee, S. M.; Lee, Y. H.; Hwang, Y. G.; Hahn, J. R.; Kang, H. *Phys. Rev. Lett.* **1999**, *82*, 217−220. (c) Szabo, T.; Berkesi, O.; Forgo, P.; Josepovits, K.; Sanakis, Y.; Petridis, D.; Dekany, I. *Chem. Mater.* **2006**, *18*, 2740−2749. (d) McAllister, M. J.; Li, J.-L.; Adamson, D. H.; Schniepp, H. C.; Abdala, A. A.; Liu, J.; Herrera-Alonso, M.; Milius, D. L.; Car, R.; Prud'homme, R. K.; Aksay, I. A. *Chem. Mater.* **2007**, *19*, 4396−4404.

(35) (a) Shin, J.; Tornquist, W. J.; Korzeniewski, C.; Hoaglund, C. S. *Surf. Sci.* **1996**, *364*, 122−130. (b) Kim, C. S.; Korzeniewski, C. *Anal. Chem.* **1997**, *69*, 2349−2353.

(36) (a) Bruce, M. I.; Humphrey, P. A.; Skelton, B. W.; White, A. H. *J. Organomet. Chem.* **1989**, *361*, 369. (b) Bruce, M. I.; Walton, J. K.; Williams, M. L.; Hall, S. R.; Skelton, B. W.; White, A. H. *J. Chem. Soc., Dalton Trans.* **1982**, 2209.

(37) (a) Granger, M. C.; Witek, M.; Xu, J.; Wang, J.; Hupert, M.; Hanks, A.; Koppang, M. D.; Butler, J. E.; Lucazeau, G.; Mermoux, M.; Strojek, J. W.; Swain, G. M. *Anal. Chem.* **2000**, *72*, 3793. (b) Xie, Y.; Anson, F. C. *J. Electroanal. Chem.* **1993**, *349*, 325.

(38) (a) Sayers, D. E.; Stern, E. A.; Lytle, F. *Phys. Rev. Lett.* **1971**, *27*, 1204. (b) Lytle, F. W.; Sayers, D. E.; Stern, E. A. *Phys. Rev. B* **1975**, *11*, 4825. (c) Stern, E. A.; Sayers, D. E.; Lytle, F. W. *Phys. Rev. B* **1975**, *11*, 4836.

(39) (a) Chupas, P. J.; Chapman, K. W.; Lee, P. L. *J. Appl. Crystallogr.* **2007**, *40*, 463−470. (b) Qiu, X.; Thompson, J. W.; Billinge, S. J. L. *J. Appl. Crystallogr.* **2004**, *37*, 678. (c) Du, P.; Kokhan, O.; Chapman, K. W.; Chupas, P. J.; Tiede, D. M. *J. Am. Chem. Soc.* **2012**, *134*, 11096−11099.

(40) (a) Billinge, S. J. L.; Kanatzidis, M. G. *Chem. Commun.* **2004**, 749. (b) Juhás, P.; Cherba, D. M.; Duxbury, P. M.; Punch, W. F.; Billinge, S. J. L. *Nature* **2006**, *440*, 655. (c) Malavasi, L. *Dalton Trans.* **2011**, *40*, 3777. (d) Chupas, P. J.; Chapman, K. W.; Chen, H. L.; Grey, C. P. *Catal. Today* **2009**, *145*, 213.

(41) Brown, P. J.; Fox, A. G.; Maslen, E. N.; M. A. O'Keeffe, Willis, B. T. M. Intensity of diffracted intensities. In *International Tables for Crystallography*; Prince, E., Ed.; John Wiley & Sons Ltd: New York, 2006; Vol. *C*, Chapter 6.1, pp 554−595

(42) Pulgarin, C.; Adler, N.; Péringer, P.; Comninellis, C. *Water Res.* **1994**, *28*, 887.

(43) Garcia Araya, J. F.; Croue, J. P.; Beltran, F. J.; Legube, B. *Ozone Sci. Eng.* **1995**, *17*, 647−656.

(44) Ciriminna, R.; Pagliaro, M. *Adv. Synth. Catal.* **2003**, *345*, 383.

(45) (a) Stonehart, P.; Kozlowska, H. A.; Conway, B. E. *Proc. R. Soc. London A* **1969**, *310*, 541. (b) Rand, D. A. J.; Woods, R. *J. Electroanal. Chem. Interfacial Electrochem.* **1974**, *55*, 375. (c) Capon, A.; Parsons, R. *J. Electroanal. Chem. Interfacial Electrochem.* **1972**, *39*, 275. (d) Buckley, D. N.; Burke, L. D. *J. Chem. Soc. Faraday Trans. 1* **1975**, *71*, 1447. (e) Pickup, P. G.; Birss, V. I. *J. Electroanal. Chem. Interfacial Electrochem.* **1987**, *220*, 83. (f) Gottesfeld, S.; Srinivasan, S. *J. Electroanal. Chem. Interfacial Electrochem.* **1978**, *86*, 89.

(46) Slavcheva, E. P. *Macedonian J. Chem. Chem. Eng.* **2011**, *30*, 45−54.

(47) Hoertz, P. G.; Kim, Y. I.; Youngblood, W. J.; Mallouk, T. E. *J. Phys. Chem. B* **2007**, *111*, 6845−6856.

(48) Sanchiz, J.; Pasan, J.; Fabelo, O.; Lloret, F.; Julve, M.; Ruiz-Perez, C. *Inorg. Chem.* **2010**, *49*, 7880−7889.

(49) (a) Zaharieva, I.; Chernev, P.; Risch, M.; Klingan, K.; Kohlhoff, M.; Fischer, A.; Dau, H. *Energy Environ. Sci.* **2012**, *5*, 7081. (b) Risch, M.; Klingan, K.; Ringleb, F.; Chernev, P.; Zaharieva, I.; Fischer, A.; Dau, H. *ChemSusChem* **2012**, *5*, 542. (c) El Wakkad, S. E. S.; Hickling, A. *Trans. Faraday Soc.* **1950**, *46*, 820. (d) Kanan, M. W.; Nocera, D. G. *Science* **2008**, *321*, 1072.

(50) (a) Nutton, A.; Bailey, P. M.; Maitlis, P. M. *J. Chem. Soc., Dalton Trans.* **1981**, 1997. (b) Dadci, L.; Elias, H.; Frey, U.; Hoernig, A.; Koelle, U.; Merbach, A. E.; Paulus, H.; Schneider, J. S. *Inorg. Chem.* **1995**, *34*, 306. (c) Ogo, S.; Makihara, N.; Watanabe, Y. *Organometallics* **1999**, *18*, 5470.

(51) Ravel, B.; Newville, M. *J. Synchrotron Radiat.* **2005**, *12*, 537−541.

(52) Newville, M. *J. Synchrotron Radiat.* **2001**, *8*, 322−324.

(53) Chupas, P. J.; Chapman, K. W.; Lee, P. L. *J. Appl. Crystallogr.* **2007**, *40*, 463−470.

(54) *Jaguar*, version 7.7; Schrodinger, LLC: New York, 2010.

(55) Becke, A. D. *J. Chem. Phys.* **1993**, *98*, 5648−5652.

(56) Lee, C.; Yang, W.; Parr, R. G. *Phys. Rev. B* **1988**, *37*, 785−789.

(57) Noodleman, L. *J. Chem. Phys.* **1981**, *74*, 5737−5743.

(58) Krishnan, R.; Binkley, J. S.; Seeger, R.; Pople, J. A. *J. Chem. Phys.* **1980**, *72*, 650−654.

(59) Bandyopadhyay, J.; Ray, S. S. *Polymer* **2010**, *51*, 1437−1449.

(60) Chantler, C. T. *J. Phys. Chem. Ref. Data* **1995**, *24*, 71−591.

(61) Rehr, J. J.; Albers, R. C. *Rev. Mod. Phys.* **2000**, *72*, 621−654.